JOURNAL OF SYNCHROTRON RADIATION
ISSN 1600-5775

A beamline-compatible STED microscope for combined visible-light and X-ray studies of biological matter

Marten Bernhardt,[a] Jan-David Nicolas,[a] Markus Osterhoff,[a] Haugen Mittelstädt,[b] Matthias Reuss,[b] Benjamin Harke,[b] Andrew Wittmeier,[a] Michael Sprung,[c] Sarah Köster[a] and Tim Salditt[a]*

[a]Institut für Röntgenphysik, Universität Göttingen, Friedrich-Hund-Platz 1, D-37077 Göttingen, Germany, [b]Abberior Instruments, Hans-Adolf-Krebs-Weg 1, D-37077 Göttingen, Germany, and [c]Deutsches Elektronen-Synchrotron (DESY), Notkestrasse 47c, D-22607 Hamburg, Germany. *Correspondence e-mail: tsaldit@gwdg.de

Received 19 October 2018
Accepted 26 March 2019

Edited by G. Grübel, HASYLAB at DESY, Germany

Keywords: STED microscope; X-ray holography; scanning SAXS; correlative microscopy; X-ray microscopy; *in situ* STED microscopy.

Supporting information: this article has supporting information at journals.iucr.org/s

A dedicated stimulated emission depletion (STED) microscope had been designed and implemented into the Göttingen Instrument for Nano-Imaging with X-rays (GINIX) at the synchrotron beamline P10 of the PETRA III storage ring (DESY, Hamburg). The microscope was installed on the same optical table used for X-ray holography and scanning small-angle X-ray scattering (SAXS). Scanning SAXS was implemented with the Kirkpatrick–Baez (KB) nano-focusing optics of GINIX, while X-ray holography used a combined KB and X-ray waveguide optical system for full-field projection recordings at a defocus position of the object. The STED optical axis was aligned (anti-)parallel to the focused synchrotron beam and was laterally displaced from the KB focus. This close proximity between the STED and the X-ray probe enabled *in situ* combined recordings on the same biological cell, tissue or any other biomolecular sample, using the same environment and mounting. Here, the instrumentation and experimental details of this correlative microscopy approach are described, as first published in our preceding work [Bernhardt *et al.* (2018), *Nat. Commun.* **9**, 3641], and the capabilities of correlative STED microscopy, X-ray holography and scanning SAXS are illustrated by presenting additional datasets on cardiac tissue cells with labeled actin cytoskeleton.

1. Introduction and overview

Imaging biological matter with hard X-rays provides a variety of unique, quantitative contrast schemes resolving structures on the nanoscale, recently down to one or two orders below the Abbe resolution limit of visible light. Multiple studies have demonstrated the benefits of hard X-ray imaging by scanning SAXS (Wilke *et al.*, 2012; Weinhausen *et al.*, 2012, 2014; Weinhausen & Köster, 2013; Hémonnot *et al.*, 2016*a*,*b*; Bernhardt *et al.*, 2016, 2017; Nicolas *et al.*, 2017*a*), coherent diffractive imaging (Rodriguez *et al.*, 2015), holography (Bartels *et al.*, 2015*a*; Krenkel *et al.*, 2015, 2016) and ptychography (Giewekemeyer *et al.*, 2010; Wilke *et al.*, 2012; Diaz *et al.*, 2015). This has all been made possible by the significant progress over the last 20 years in X-ray focusing (Schroer *et al.*, 2005; Hignette *et al.*, 2005; Mimura *et al.*, 2010; Chao *et al.*, 2009; Paganin, 2006; Attwood & Sakdinawat, 2017), analysis of diffraction data (Lichtenegger *et al.*, 1999; Bunk *et al.*, 2009; Liebi *et al.*, 2015), as well as reconstruction algorithms for coherent imaging (Cloetens *et al.*, 1999; Miao *et al.*, 1999; Paganin, 2006; Nugent, 2010; Krenkel *et al.*, 2017). However,

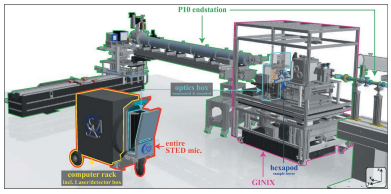

© 2019 International Union of Crystallography

in particular for scanning SAXS, data interpretation remains a tremendous challenge when probing objects as complex as a biological cell, because the detected signal originates from the entire ensemble of biomolecular constituents and is resolved only along two dimensions. This makes it difficult to directly trace back contributions of the detected signal to a single, specific component.

Here, we focus on complementing hard X-ray imaging, more precisely X-ray inline holography and scanning SAXS, with super-resolution visible-light fluorescence microscopy. In fluorescence microscopy the detected signal originates from fluorophores bound to a target molecule. By this approach, only structures which are specifically labeled become visible in the corresponding micrographs, which is a particular advantage but at the same time a great limitation. With the advent of super-resolution microscopy (nanoscopy), the resolution of fluorescence micrographs can be significantly enhanced beyond the Abbe limit (Hell, 2007; Rust *et al.*, 2006; Betzig *et al.*, 2006). Based on switching between emissive (bright) and non-emissive (dark) states of the fluorophore, biological structures down to the nanoscale have become accessible. In the present work, we use stimulated emission depletion (STED) microscopy as one of the most advanced super-resolution techniques, well matched to the minimum structure size, which can be resolved by X-ray holography (Bartels *et al.*, 2015*b*) and scanning SAXS (Priebe *et al.*, 2014). By correlating STED and X-ray data we exploit the synergistic effects of all three imaging modalities in order to obtain a more complete view of the same biological cell. In this way, different subcomponents of a cell can be localized one after the other, and then be set in relation to the entire ensemble of components as visualized by X-ray holographic phase maps. For this combined approach we take advantage of the integrated STED configuration, which is required to quickly switch between the STED and any X-ray modality by simple lateral translation of the sample tower. Data in all three modalities can be acquired in any sequential order.

Fig. 1 illustrates the three imaging modalities, as sketched from left to right.

For STED microscopy (red box), the sample is translated into the focal spot of a high numerical aperture (NA) air objective. Fluorophores in the object plane are stimulated by an excitation laser at around $\lambda_{exc} = 632$ nm [see upper part and inset (1) of Fig. 1]. The depletion pulse at $\lambda_{depl} = 775$ nm is shaped by a set of waveplates exploiting polarization [denoted as the 'easySTED' unit; see Reuss (2011), Reuss *et al.* (2010)], which results in a donut-shape of the STED intensity profile in the focal plane of the STED objective. Fluorophores can be depleted within the entire annulus around the central zero by stimulated emission, so that the effective spot size of the remaining emission in the center of the probing spot is smaller than the limit defined by the Abbe resolution criterion. Excitation and depletion pulses are separated by a time delay of a few hundred picoseconds. For a STED recording, the object is probed in a raster scan, by lateral piezo translation of the objective along the *y*- and *z*-directions. In addition, the objective can also be scanned along the *x*-direction (*i.e.* the STED beam axis), *e.g.* for the recording of 3D confocal or STED stacks. The signal is detected with respect to the scan position by a single-photon-counting diode. The sample, mounted on a motorized stage, is placed in the focal plane of the objective. In the recent, already upgraded setup, a hexapod nano-positioning system is used for translation of the sample. Its three translational and three rotational degrees of freedom enable aligning the object plane of the sample parallel to the focal plane of the objective [see Fig. 1 (lower part)]. All instrumentation details, as well as the implementation of the STED microscope, are further described in Sections 2 and 3. For switching between STED and X-ray imaging, the object is laterally transferred by about 30 cm between STED and X-ray focus, which is currently realized by a long translation rail underneath the hexapod.

For holography (blue box), the monochromated undulator-generated X-ray beam is focused by a set of Kirkpatrick–Baez (KB) mirrors and coupled into a waveguide, which is aligned in the KB focus for coherence filtering. The object is placed at a defocus position z_1 in the emanating wavefront. Density variations within the object lead to wavefront distortions [see the dashed green bows in inset (2)]. Self-interference with the primary beam behind the object (Huygen's principle) converts phase distortions to a measurable intensity pattern, the so-called inline hologram, which is detected at distance z_2 by an sCMOS camera (2048 × 2048 pixels, Photonic Science). X-ray holography is a full-field method and the field of view can be tuned to the object size by variation of the geometrical magnification defined by distances z_1 and z_2. An on-axis video microscope (OAV) facilitates navigation and (re-)identification of regions of interest (ROIs).

With all holographic recordings completed, the instrument settings are switched from X-ray holography to scanning SAXS, as previously reported by Nicolas *et al.* (2017*b*). To this end, the waveguide is removed from the beam axis, apertures and beamstops are aligned for scanning SAXS, and the sample is moved into the KB focus. The sCMOS camera is replaced by the Pilatus 300K single-photon-counting detector (Dectris). Fig. 1 (green box) shows the basic setup for scanning SAXS. Soft-edge apertures are placed between the KB mirrors and the object in order to clean parasitic scattering tails of the primary beam. The primary beam is blocked by a rectangular beamstop behind the object. Scattered photons are recorded on the same detector bench as for X-ray holography, which is approximately 5 m downstream from the object. The object is then rastered by a motorized stage through the beam [see also the inset (3)], resulting in an array of 2D diffraction patterns.

This manuscript is organized as follows. After this brief introduction, the STED microscope, with its main optical components, is detailed in Section 2. Next, the implementation of the microscope into the GINIX instrument is described in Section 3. Research examples on cardiac tissue cells are presented in Section 4. Section 5 closes the manuscript by summarizing the present status of the instrumentation and by outlining the next steps for possible upgrades and applications.

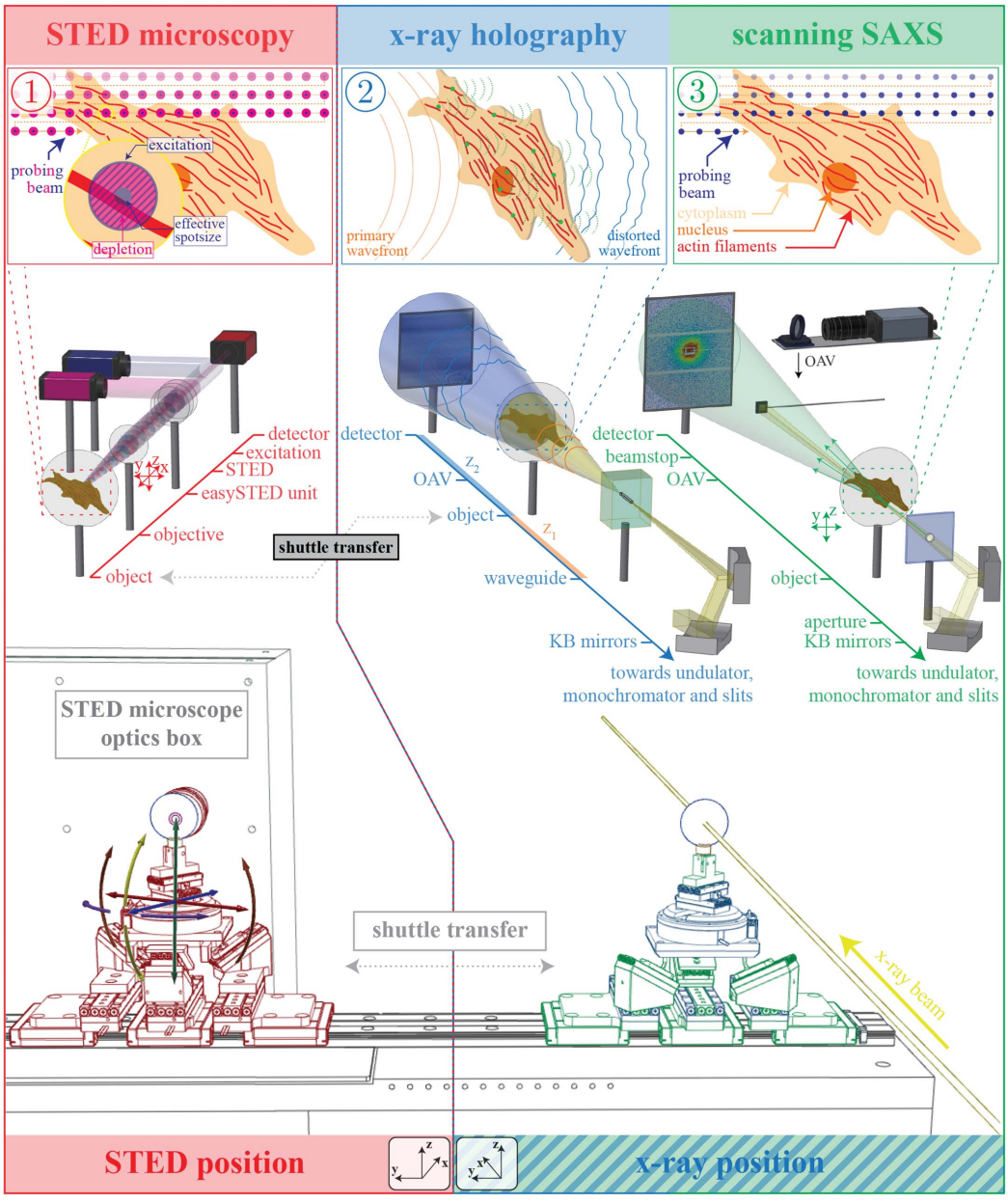

Figure 1
Sketch illustrating the setup and the recording principle for the combined imaging approach using STED microscopy (red box), X-ray holography (blue box) and scanning SAXS (green box). Upper and central part: main components of the setup together with illustrations of the respective recording principles. Lower part: hexapod sample stage and translation rail realizing the shuttle transfer of the sample between the STED and the X-ray recording position.

2. Optics and construction of the STED microscope

The STED microscope consists of (i) a computer rack including the control computer and a *laser and detector box*, which houses the excitation laser, the STED laser as well as the avalanche photodiode (APD), and (ii) an *optics box*, which includes all further optical components. The microscope provides two basic operation modes: the scanning mode is applied for confocal and STED microscopy, utilizing the lasers and photodiode placed inside the *laser and detector box*; furthermore, a full-field mode is available, which can be operated with either epifluorescence or bright-field illumination. All optical components for full-field imaging are installed in the *optics box*.

Fig. 2 shows sketches of the *laser and detector box* [see Fig. 2A], as well as the *optics box* (see Fig. 2B). For STED microscopy (scanning mode), the (*a*) excitation and (*b*) STED beam (blue and pink lines) are coupled into the beam path by two (*c*) acousto-optic modulators (AOMs). With the AOMs set active, the beams are guided through the adjacent (*d*) apertures. Both AOMs are connected to the internal interlock system. Two additional mechanical safety shutters provide extra safety, so that the microscope can be operated as a standalone instrument at any synchrotron beamline.

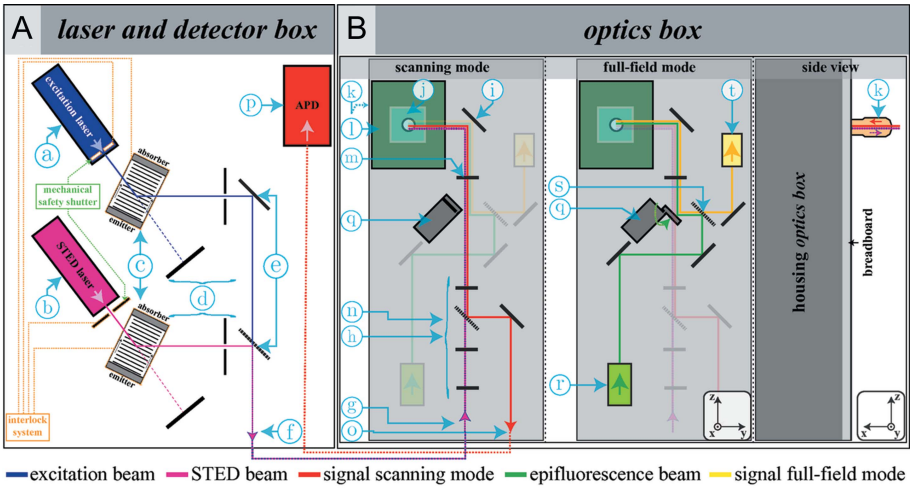

Figure 2
Sketches of the (A) laser and detector box and the (B) optics box. Markers denote: (*a*) excitation laser and (*b*) STED laser, (*c*) acousto-optic modulators, (*d*) apertures, (*e*) adjustable mirrors, (*f*) glass fiber cable front end in the laser and detector box, (*g*) glass fiber cable back end in the optics box, (*h*) easySTED unit, (*i*)–(*j*) additional guiding mirrors, (*k*) STED microscope objective, (*l*) *xyz*-piezo stage, (*m*) tubus lens, (*n*) dichroic mirror, (*o*) position towards the photodiode (*i.e.* front end of the second glass fiber cable inside the optics box), (*p*) photodiode, (*q*) motorized flippable mirror, (*r*) epifluorescence-LED, (*s*) dichroic mirror/emission filter for full-field mode and (*t*) CCD camera.

Next, a set of (*e*) adjustable mirrors superimpose the laser pulses spatially (but not temporally) and couple them into a (*f*) glass fiber cable. The cable guide the beams from the *laser and detector box* towards position (*g*) in the *optics box*. The (*h*) 'easySTED' unit composed of an achromatic quarter-wave plate, a chromatic segmented wave plate and an achromatic half-wave plate (Reuss *et al.*, 2010; Reuss, 2011) shapes the STED beam into a donut profile in focus of the (*k*) STED ∞-objective (UPLSAPO 40 × 2, Olympus). The beams are guided by two mirrors at position (*i*)–(*j*). Scanning is realized by a (*l*) nano-positioning stage translating the objective with respect to the sample. The photons emitted by the sample (red line) are focused by a (*m*) tubus lens and separated from the probing beam path by a (*n*) dichroic mirror serving as the scanning mode emission filter (F47-686, AHF Analysetechnik). The signal is coupled into a second glass fiber at position (*o*) and single photons from each scan position are recorded by an (*p*) APD back in the *laser and detector box*.

For epifluorescence full-field mode, a (*q*) motorized mirror is flipped, guiding the (*r*) internal epifluorescence LED to the (*k*) objective (green line). The emitted photons (yellow line) are separated from the probing beam path by a (*s*) dichroic mirror which serves as the epifluorescence emission filter (F33-633, AHF Analysetechnik). Photons are recorded by a CCD camera (DMK23U274, Sony) at position (*t*). For bright-field microscopy, we use the LED transillumination, as discussed in Section 3 and presented in Fig. S2 of the supporting information (SI). The field of view is about 130 µm × 175 µm in full-field mode and about 100 µm × 100 µm in scanning mode. Specifications of the installed lasers and epifluorescence LED are listed in Table S1 of the SI.

For a sample recording, the typical workflow is as follows. The sample is first inspected in bright-field mode. By video monitoring, a ROI is selected. The sample is coarsely aligned to the focal plane. Next, the fluorescence signal is judged in epifluorescence mode, followed by coarsely rastered view scans (step size typically 200 nm) including line scans along the optical axis. After having moved to an appropriate sample position in the focal plane, a combined confocal and STED scan is recorded with a typical step size of around 30 nm. For further illustration of the four recording modes, see Section S2, as well as Fig. S2 and Figs. S6–S8 of the SI.

So far, the STED microscope, as introduced here, is limited to a single fluorescence channel. Nevertheless, due to the flexible modular setup, upgrading the instrument towards more fluorescence channels is possible. For the present setup, appropriate dyes are, for example, Atto633, Atto647N, AlexaFluor647 and AbberiorSTAR635. For future living cell measurements, fluorescent proteins, which match the requirements of the microscope, are already commercially available. After stable transfection of the corresponding coding DNA into a cell line, these proteins would enable recordings of target structures in the living cell (Matela *et al.*, 2017; Hense *et al.*, 2015).

3. Instrumentation and implementation into GINIX

Fig. 3 outlines the installation of the STED microscope into the GINIX instrument. The microscope is transferred to the beamline in a wheeled cart [see Fig. 3(*a*)]. The *optics box* is installed to the left of the X-ray beam on the optical table of the GINIX instrument. Figs. 3(*b*)–3(*c*) show sketches of the side and top view of this configuration, and Fig. 3(*d*) presents a photograph taken during the first beam time. The *laser and detector box* of the (1) computer rack and the (3) *optics box* are connected by the two (2) glass fiber cables of about 10 m in length. The (4) STED objective of the *optics box* is aligned anti-parallel to the X-ray beam axis. The sample is glued on a brass pin and then mounted on the (5) motorized sample tower. Recording modes are switched by translation of the sample tower along the *y*-direction, here realized by a (6) PI long-range linear translation stage. A (7) granite block below the sample stage minimizes vibrations.

Before STED recordings, a (8) safety box is placed on top of the sliding carriage for safety purposes. Contact switches ensure feedback to the internal interlock system, so that no beam can exit the *laser and detector box* whenever the safety cap is off. White-light LEDs installed at the back of the safety cap enable bright-field illumination of the sample [see also

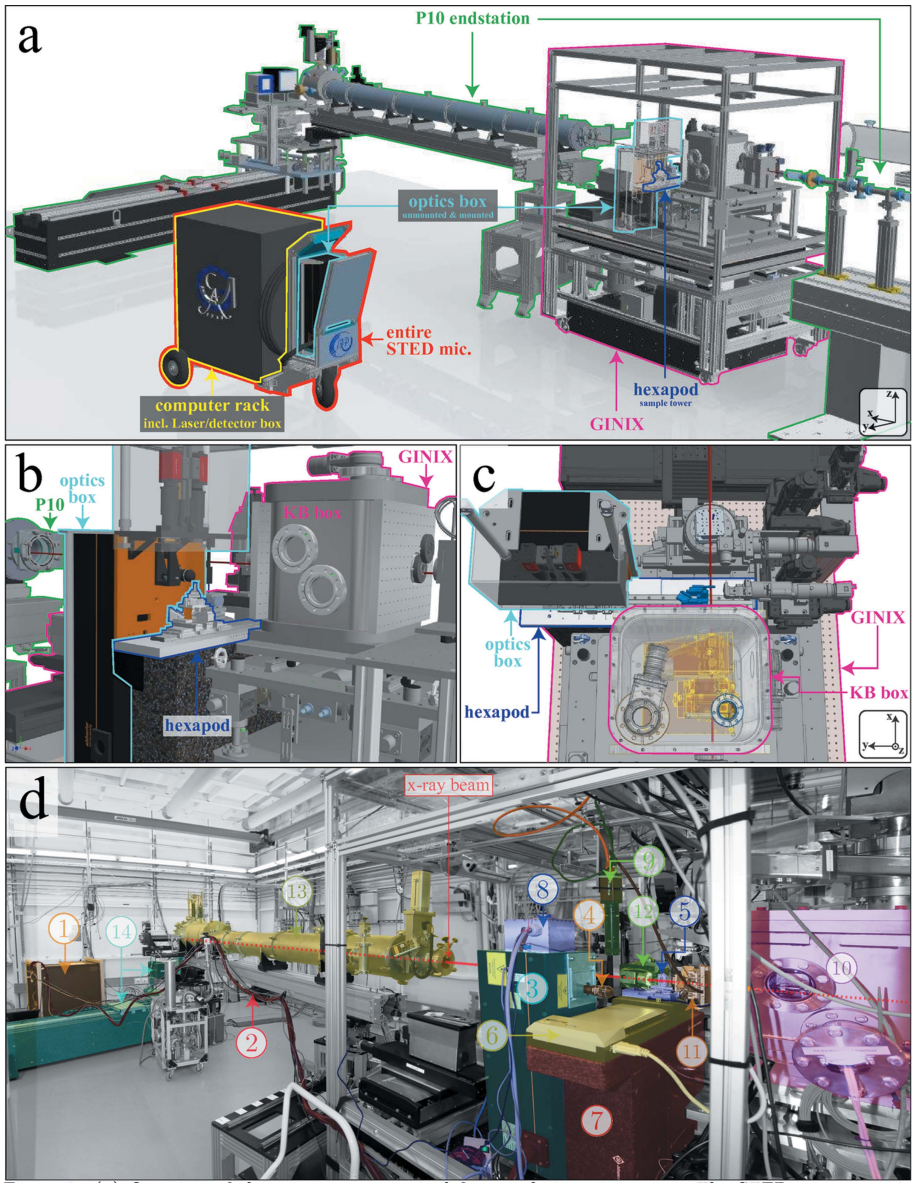

Figure 3
(*a*) Overview of the components. The STED microscope is transferred to the beamline on a wheeled cart and consists of a computer rack including the laser and detector box and the optics box. (*b*)–(*c*) Side and top view of the integrated setup at the sample recording positions. The optics box is installed left and anti-parallel to the X-ray beam axis. (*d*) Photograph of the integrated STED and X-ray setup during the first synchrotron beam time. (1) STED microscope rack, (2) glass fiber cable, (3) optics box, (4) STED microscope objective, (5) sample and motorized tower, (6) stepping motor for *y*-translation, (7) granite blocks, (8) safety box and bright-field illumination, (9) top-view video camera, (10) KB box, (11) waveguide and *xyz*-mount, (12) on-axis video camera, (13) evacuated tube, (14) X-ray detectors and bench. Adapted from Bernhardt *et al.* (2018).

Fig. S2(*i*)]. A (9) vertical video-microscope (Manta G-146 camera, Allied Vision) equipped with a high-magnification adapter (Navitar) monitors the current distance between the objective and the sample (see also Fig. S2). This is necessary to prevent collisions of the sample with the STED objective, since high NA-objectives require a small working distance of a few hundred micrometres. The recent, upgraded version of the setup provides a second, horizontal video microscope, so that with top and side views available the sample can be pre-positioned and tilts can already be roughly corrected by using the hexapod's rotational degrees of freedom. The KB mirrors used for X-ray nano-focusing are placed inside an (10) evacuated box, focusing the beam down to 300 nm to 400 nm. For X-ray holography experiments, an X-ray waveguide is positioned on a vertical hexapod, see (11), mounted on top of the exit window of the KB box. Before the X-ray recording, a ROI is identified by using the (12) OAV. After impinging on the sample, X-ray photons propagate through an (13) evacuated tube, which spans a sample–detector distance of about 5 m, thus minimizing air scattering. The signal is recorded by the detectors mounted on the (14) motorized detector bench.

4. Research examples

In a first proof-of-principle study we investigated neonatal rat cardiac tissue cells (NRCTCs) with a fluorescently labeled actin cytoskeleton. In order to simplify sample handling at the beamline and to enhance the X-ray contrast, cells were freeze-dried before imaging. The sample preparation was the same as described in our preceding work (Bernhardt *et al.*, 2018). Neonatal rat cardiac tissue cells were obtained from one to two days old neonatal Wistar rats. Ventricles were sliced in phosphate buffer, followed by three to four digestion steps with collagenase II (300 U ml^{-1}, Worthington, 15 min at 310 K) and centrifugation [see also Richter & Luther (2010) and Rother *et al.* (2015)]. A glass coverslip serving as the substrate (thickness #1, corresponding to 0.13–0.16 mm) was plasma-cleaned for several minutes. It was then transferred to a 12-well plate under a clean bench and coated with a fibronectin/gelatin-solution (F4759 and G7041, Sigma-Aldrich). The well was flooded with a cell suspension of 2×10^5 cells ml^{-1} in medium (DMEM-F12, 11039-021, Gibco; 10% FCS, 10270-106, Gibco; 1% pen./strep. 15140-122, Gibco) until the substrate was fully covered. The sample was then transferred into the cell incubator (310 K, 5% CO_2) allowing the cells to adhere on the substrate. The adhered cells were fixed the next day using 9% formaldehyde (252549, Sigma-Aldrich) in Dulbecco's phosphate-buffered saline (DPBS D8537, Sigma-Aldrich). They were then permeabilized with Triton X-100 and the actin filaments were labeled with a solution of 0.5 µ*M* Phalloidin-

Atto633 (AD 633-8X, Atto-Tec) in DPBS following manufacturer protocols. Samples were plunged into an ultracool bath (tempered at around 80 K) of a liquid ethane/propane mixture using a Leica GP EM grid plunging system. Samples were then transferred into a home-built lyophilizator and freeze-dried.

All data were recorded during a single beam time at beamline P10 of PETRA III, DESY, using the GINIX instrument at an X-ray photon energy of 13.8 keV. The photon flux in focus was $I_0 \simeq 1.1 \times 10^{11}$ photons s^{-1} and the beam size was determined to be around 290 nm × 340 nm (horizontal × vertical direction, FWHM) (see also Fig. S3). For X-ray beam attenuation, if required, a set of 50–400 µm-thick molybdenum foils was used. Holographic recordings were performed at a single distance between the waveguide and the sample, with $z_1 \simeq 25$ mm and $z_2 \simeq 5$ m. For practical reasons, the sample was placed with the cells facing upstream towards the X-ray source. In this way, the correction ring of the STED objective (aligned anti-parallel to the incoming X-rays) can simply be adjusted to the thickness of the glass substrate, thus correcting aberrations.

Fig. 4 presents datasets of the different imaging modalities. Figs. 4(*a*)–4(*b*) show the confocal overview, see (*a*), and STED micrograph around the cellular nucleus, see (*b*), on a single NRCTC. Actin filaments follow the main elongation axis of the cell. The phase map as obtained from a contrast transfer function (CTF) reconstruction of the X-ray holography data, see Fig. 4(*c*), reveals cellular structures including the nucleus, which are invisible in the fluorescence micrographs of Figs. 4(*a*)–4(*b*).

Fig. 4(*d*) shows the scanning SAXS map of the same cell, *i.e.* the so-called X-ray darkfield image, recorded with the KB-focused X-ray beam, along with illustrative far-field diffraction patterns (inset). The darkfield image is computed by 2D integration of photon counts on the detector, after excluding primary beam intensity contributions by applying a logical mask to the signal [see also Fig. S9]. In this contrast, the nucleus, which appears with a rather strong scattering signal, can be separated from cytoplasmic regions and from the background signal. Fig. 4(*e*) shows the results of a principal component analysis (PCA) quantifying the anisotropy of the diffraction signal as caused by elongated, filamentous structures. For PCA, we have background-corrected the diffraction data and filled up missing detector gaps by symmetry operations (Nicolas *et al.*, 2017*a*; Nicolas, 2017). The anisotropy parameter ω is derived from the highest and lowest variance $\lambda_{1,2}$ of the momentum transfer, *i.e.* $\omega = |\lambda_1 - \lambda_2|/(\lambda_1 + \lambda_2)$ [see also Bernhardt *et al.* (2016)]. The structure orientation thresholded to darkfield values above 7.075×10^5 photons s^{-1} is indicated by green lines.

Fig. 5 presents another example showing the confocal overview in (*a*), and a combined confocal and STED scan in (*b*). Fig. 5(*c*) shows a CTF-based phase reconstruction of a 4 × 4 array of holographic images. The STED signal, the holographic phase shifts and the overall SAXS signal (see also Fig. S11), reveal significant variations between different cells. One possible explanation is that in some cases an adherent and a non-adherent cell are stacked on top of each other. In this case, the local variation of the phase shift in the holographic signal can become too strong (in particular the phase

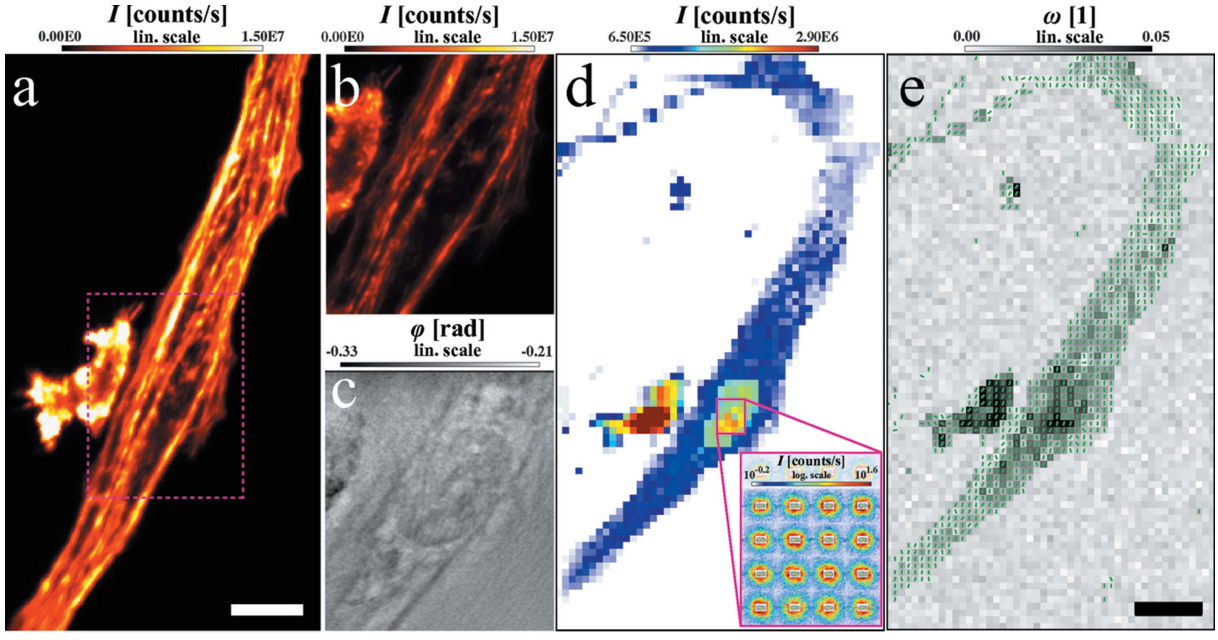

Figure 4
(*a*) Confocal overview and (*b*) STED micrograph of a freeze-dried neonatal rat cardiac tissue cell. Scale bar: 10 µm. (*c*) CTF-based phase reconstruction on X-ray holography data showing the same zoom as in (*b*). (*d*) X-ray darkfield map as computed from the scanning SAXS data of the cell. The inset shows 2D diffraction patterns around the nucleic region of the cell. (*e*) PCA on the 2D diffraction patterns showing the principal structure direction and degree of anisotropy of filamentous structures. Scale bar: 10 µm.

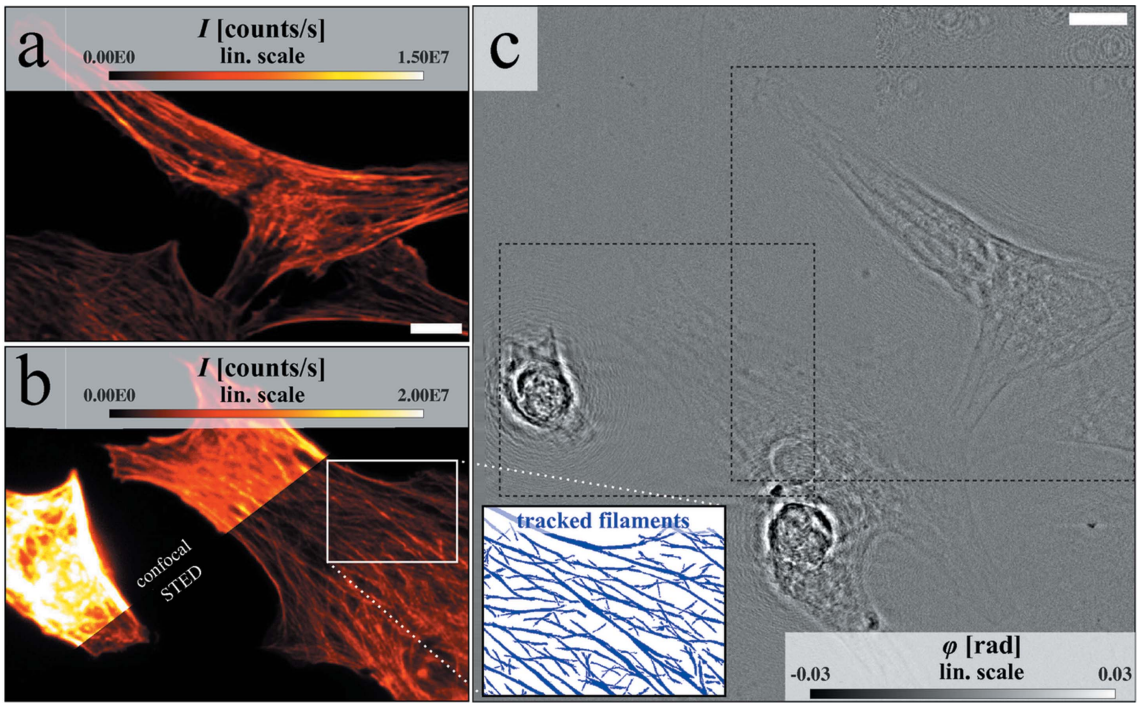

Figure 5
(*a*)–(*b*) Confocal overview as well as combined confocal and STED micrographs of two sample ROIs. The quality of the STED micrograph of (*b*) allows to track the most significant filaments as found by the so-called filament sensor (Eltzner *et al.*, 2015), see inset (blue lines). Scale bar: 10 µm. (*c*) CTF-based phase reconstruction of X-ray holograms recorded at a single distance. The area shown results from a 4 × 4 stitch of holograms recorded at different lateral positions on the sample area. Scale bar: 10 µm.

gradient), so that the assumption of a weakly varying phase required for CTF phase retrieval must be questioned. This might also explain the residual edge enhancement in the reconstructions shown in Fig. 5(*c*).

The data quality of the STED/confocal fluorescence micrographs allows to reliably track the most significant actin filaments and filament bundles with automated filament detection algorithms. This is demonstrated in Fig. 5(*b*), where the inset shows a segmentation of filaments using the filament sensor algorithms from Eltzner *et al.* (2015). In this way, a structure orientation is assigned to each pixel position. As we have demonstrated elsewhere (Bernhardt *et al.*, 2018), the filament sensor algorithm can also be applied to the holographic phase maps. After numerical rebinning, the pixelwise agreement between STED and holographic data can be evaluated in a quantitative manner [see also Bernhardt *et al.* (2018)].

5. Summary and outlook

Here, we have described the details of design, construction and implementation of the first *in situ* STED microscope, which has been installed on the optical table of a synchrotron endstation instrument. The dedicated design with the STED optical axis aligned (anti-)parallel to the X-ray beam enables *in situ* correlative recordings, combining STED microscopy with the various X-ray imaging modalities provided by the X-ray instrument. Based on the correlation of datasets, a fluorescently labeled target structure of interest, as derived from the STED fluorescence data, can be localized in the X-ray data, which visualize the entire ensemble of cellular structures regardless of labeling. By this combination of imaging methods, contributions from the X-ray signal can be assigned to a specific cellular substructure, as derived from the STED data, and one can detect the background structure, in which the labeled moiety is embedded.

For the future, many different extensions and applications are possible. For example, topics such as the tolerable radiation dose for living cells and, facilitated by X-ray-compatible microfluidic chambers (Weinhausen & Köster, 2013; Denz *et al.*, 2018), the recording of dynamic biological processes with STED and X-ray microscopy can be addressed with this setup. These projects explicitly require the *in situ* configuration of the STED microscope, because especially living state measurements are often time-critical, and only a close proximity between both the STED and X-ray instrument can keep the time span between exposures to a minimum. Furthermore, it is possible to extend this correlative approach to three dimensions by recording STED stacks of a cell and combine this information with X-ray data from tomographic recordings.

Acknowledgements

We thank Stefan Hell for continuous support and advice, Susanne Hengst for help with cell culture, Matthias Meister, Peter Luley and Bastian Hartmann for engineering support,

Anna-Lena Robisch for help with holographic reconstruction algorithms, Benjamin Eltzner for software support and Stefan Luther and Marion Kunze for providing heart tissue cells.

Funding information

Funding for this research was provided by: Deutsche Forschungsgemeinschaft (grant No. SFB937; projects A07, A11 and A12) for funding the correlative microscopy of actin cytoskeleton networks and Bundesministerium für Bildung und Forschung (grant No. 05K16MG2) for funding of the custom-built STED microscope.

References

Attwood, D. & Sakdinawat, A. (2017). *X-rays and Extreme Ultraviolet Radiation: Principles and Applications.* Cambridge University Press.

Bartels, M., Krenkel, M., Cloetens, P., Möbius, W. & Salditt, T. (2015*a*). *J. Struct. Biol.* **192**, 561–568.

Bartels, M., Krenkel, M., Haber, J., Wilke, R. N. & Salditt, T. (2015*b*). *Phys. Rev. Lett.* **114**, 048103.

Bernhardt, M., Nicolas, J.-D., Eckermann, M., Eltzner, B., Rehfeldt, F. & Salditt, T. (2017). *New J. Phys.* **19**, 013012.

Bernhardt, M., Nicolas, J.-D., Osterhoff, M., Mittelstädt, H., Reuss, M., Harke, B., Wittmeier, A., Sprung, M., Köster, S. & Salditt, T. (2018). *Nat. Commun.* **9**, 3641.

Bernhardt, M., Priebe, M., Osterhoff, M., Wollnik, C., Diaz, A., Salditt, T. & Rehfeldt, F. (2016). *Biophys. J.* **110**, 680–690.

Betzig, E., Patterson, G. H., Sougrat, R., Lindwasser, O. W., Olenych, S., Bonifacino, J. S., Davidson, M. W., Lippincott-Schwartz, J. & Hess, H. F. (2006). *Science*, **313**, 1642–1645.

Bunk, O., Bech, M., Jensen, T. H., Feidenhans'l, R., Binderup, T., Menzel, A. & Pfeiffer, F. (2009). *New J. Phys.* **11**, 123016.

Chao, W., Kim, J., Rekawa, S., Fischer, P. & Anderson, E. H. (2009). *Opt. Express*, **17**, 17669–17677.

Cloetens, P., Ludwig, W., Baruchel, J., Van Dyck, D., Van Landuyt, J., Guigay, J. P. & Schlenker, M. (1999). *Appl. Phys. Lett.* **75**, 2912–2914.

Denz, M., Brehm, G., Hémonnot, C. Y. J., Spears, H., Wittmeier, A., Cassini, C., Saldanha, O., Perego, E., Diaz, A., Burghammer, M. & Köster, S. (2018). *Lab Chip*, **18**, 171–178.

Diaz, A., Malkova, B., Holler, M., Guizar-Sicairos, M., Lima, E., Panneels, V., Pigino, G., Bittermann, A. G., Wettstein, L., Tomizaki, T., Bunk, O., Schertler, G., Ishikawa, T., Wepf, R. & Menzel, A. (2015). *J. Struct. Biol.* **192**, 461–469.

Eltzner, B., Wollnik, C., Gottschlich, C., Huckemann, S. & Rehfeldt, F. (2015). *PLoS ONE*, **10**, e0126346.

Giewekemeyer, K., Thibault, P., Kalbfleisch, S., Beerlink, A., Kewish, C. M., Dierolf, M., Pfeiffer, F. & Salditt, T. (2010). *Proc. Natl Acad. Sci.* **107**, 529–534.

Hell, S. W. (2007). *Science*, **316**, 1153–1158.

Hémonnot, C. Y. J., Ranke, C., Saldanha, O., Graceffa, R., Hagemann, J. & Köster, S. (2016*a*). *ACS Nano*, **10**, 10661–10670.

Hémonnot, C. Y. J., Reinhardt, J., Saldanha, O., Patommel, J., Graceffa, R., Weinhausen, B., Burghammer, M., Schroer, C. G. & Köster, S. (2016*b*). *ACS Nano*, **10**, 3553–3561.

Hense, A., Prunsche, B., Gao, P., Ishitsuka, Y., Nienhaus, K. & Nienhaus, G. U. (2015). *Sci. Rep.* **5**, 18006.

Hignette, O., Cloetens, P., Rostaing, G., Bernard, P. & Morawe, C. (2005). *Rev. Sci. Instrum.* **76**, 063709.

Krenkel, M., Markus, A., Bartels, M., Dullin, C., Alves, F. & Salditt, T. (2015). *Sci. Rep.* **5**, 9973.

Krenkel, M., Toepperwien, M., Alves, F. & Salditt, T. (2017). *Acta Cryst.* A**73**, 282–292.

Krenkel, M., Töpperwien, M., Dullin, C., Alves, F. & Salditt, T. (2016). *AIP Adv.* **6**, 035007.

Lichtenegger, H., Müller, M., Paris, O., Riekel, C. & Fratzl, P. (1999). *J. Appl. Cryst.* **32**, 1127–1133.

Liebi, M., Georgiadis, M., Menzel, A., Schneider, P., Kohlbrecher, J., Bunk, O. & Guizar-Sicairos, M. (2015). *Nature*, **527**, 349–352.

Matela, G., Gao, P., Guigas, G., Eckert, A. F., Nienhaus, K. & Ulrich Nienhaus, G. (2017). *Chem. Commun.* **53**, 979–982.

Miao, J., Charalambous, P., Kirz, J. & Sayre, D. (1999). *Nature*, **400**, 342–344.

Mimura, H., Handa, S., Kimura, T., Yumoto, H., Yamakawa, D., Yokoyama, H., Matsuyama, S., Inagaki, K., Yamamura, K., Sano, Y., Tamasaku, K., Nishino, Y., Yabashi, M., Ishikawa, T. & Yamauchi, K. (2010). *Nat. Phys.* **6**, 122–125.

Nicolas, J.-D. (2017). *Nanodiffraction Toolbox*, https://irpgoe.github.io/nanodiffraction/.

Nicolas, J.-D., Bernhardt, M., Krenkel, M., Richter, C., Luther, S. & Salditt, T. (2017*b*). *J. Appl. Cryst.* **50**, 612–620.

Nicolas, J.-D., Bernhardt, M., Markus, A., Alves, F., Burghammer, M. & Salditt, T. (2017*a*). *J. Synchrotron Rad.* **24**, 1163–1172.

Nugent, K. A. (2010). *Adv. Phys.* **59**, 1–99.

Paganin, D. (2006). *Coherent X-ray Optics*, No. 6. Oxford University Press on Demand.

Priebe, M., Bernhardt, M., Blum, C., Tarantola, M., Bodenschatz, E. & Salditt, T. (2014). *Biophys. J.* **107**, 2662–2673.

Reuss, M. (2011). PhD thesis, University of Heidelberg, Germany.

Reuss, M., Engelhardt, J. & Hell, S. W. (2010). *Opt. Express*, **18**, 1049–1058.

Richter, C. & Luther, S. (2010). *Biomed. Tech.* **55**, S1.

Rodriguez, J. A., Xu, R., Chen, C.-C., Huang, Z., Jiang, H., Chen, A. L., Raines, K. S., Pryor Jr, A., Nam, D., Wiegart, L., Song, C., Madsen, A., Chushkin, Y., Zontone, F., Bradley, P. J. & Miao, J. (2015). *IUCrJ*, **2**, 575–583.

Rother, J., Richter, C., Turco, L., Knoch, F., Mey, I., Luther, S., Janshoff, A., Bodenschatz, E. & Tarantola, M. (2015). *Open Biol.* **5**, 150038.

Rust, M. J., Bates, M. & Zhuang, X. (2006). *Nat. Methods*, **3**, 793–795.

Schroer, C. G., Kurapova, O., Patommel, J., Boye, P., Feldkamp, J., Lengeler, B., Burghammer, M., Riekel, C., Vincze, L., van der Hart, A. & Küchler, M. (2005). *Appl. Phys. Lett.* **87**, 124103.

Weinhausen, B. & Köster, S. (2013). *Lab Chip*, **13**, 212–215.

Weinhausen, B., Nolting, J.-F., Olendrowitz, C., Langfahl-Klabes, J., Reynolds, M., Salditt, T. & Köster, S. (2012). *New J. Phys.* **14**, 085013.

Weinhausen, B., Saldanha, O., Wilke, R. N., Dammann, C., Priebe, M., Burghammer, M., Sprung, M. & Köster, S. (2014). *Phys. Rev. Lett.* **112**, 088102.

Wilke, R. N., Priebe, M., Bartels, M., Giewekemeyer, K., Diaz, A., Karvinen, P. & Salditt, T. (2012). *Opt. Express*, **20**, 19232–19254.